

Article

# Numerical and Experimental Investigations on Non-Linear Wave Action on Offshore Wind Turbine Monopile Foundation

Sijia Deng <sup>1,2</sup>, Ming Qin <sup>3</sup>, Dezhi Ning <sup>1,2,\*</sup>, Lin Lin <sup>3</sup>, Songxiong Wu <sup>3</sup> and Chongwei Zhang <sup>1,2,\*</sup>

<sup>1</sup> State Key Laboratory of Coastal and Offshore Engineering, Dalian University of Technology, Dalian 116024, China

<sup>2</sup> Dalian Key Laboratory of Offshore Renewable Energy, Dalian University of Technology, Dalian 116024, China

<sup>3</sup> Science and Technology Research Institute, China Three Gorges Corporation, Beijing 100038, China

\* Correspondence: dzning@dlut.edu.cn (D.N.); chongweizhang@dlut.edu.cn (C.Z.)

**Abstract:** Monopiles are commonly utilized in offshore wind farms but are prone to non-linear wave loads and run-ups, significantly affecting their engineering design. Therefore, it is crucial to pursue a complete understanding of the non-linear wave action on monopile foundations. Both numerical and experimental investigations on the non-linear wave loads and run-ups on an offshore wind turbine monopile foundation are performed in this paper. The experiment is carried out at a scale of 1/30 in a wave flume at the State Key Laboratory of Coastal and Offshore Engineering, Dalian University of Technology, in which the wave loads and run-ups along the monopile are measured. Based on the second-order potential flow model and time-domain higher-order boundary element method (HOBEM), the related numerical tests are conducted to study the non-linear effects further. It is found that the present non-linear potential theory is sufficient for the simulation of wave force and run-ups on the monopile in the range of wave slope  $kA < 0.15$  before wave breaking. “W” type distribution of wave run-up along the monopile is found, in which the peak value occurs at the frontward side (i.e.,  $\theta = 180^\circ$ ) and is the maximum due to full reflection; the two symmetrical minimum amplitudes lie in the zones of  $(45^\circ \leq \theta \leq 90^\circ)$  and  $(270^\circ \leq \theta \leq 315^\circ)$ , whose positions shift downward with the increase of wave non-linearity. Energy transfer among the fundamental wave component and higher-order components is also found, which is most apparent on the backward side. Besides, the transverse resonance occurs in the wave flume due to the wavelength being near the flume width, which induces the wave run-up at the backward position larger than that at the frontward position.

**Keywords:** offshore wind turbine monopile; non-linear wave loads; HOBEM; run-up; physical experiment



**Citation:** Deng, S.; Qin, M.; Ning, D.; Lin, L.; Wu, S.; Zhang, C. Numerical and Experimental Investigations on Non-Linear Wave Action on Offshore Wind Turbine Monopile Foundation. *J. Mar. Sci. Eng.* **2023**, *11*, 883. <https://doi.org/10.3390/jmse11040883>

Academic Editor: Jens Engström

Received: 12 March 2023

Revised: 15 April 2023

Accepted: 18 April 2023

Published: 21 April 2023



**Copyright:** © 2023 by the authors. Licensee MDPI, Basel, Switzerland. This article is an open access article distributed under the terms and conditions of the Creative Commons Attribution (CC BY) license (<https://creativecommons.org/licenses/by/4.0/>).

## 1. Introduction

In recent years, the global goal of achieving carbon neutrality to combat the energy crisis and climate change has gained significant momentum. Offshore wind energy has emerged as a fast-growing clean energy source, with 21 GW out of 94 GW of wind turbines installed offshore [1]. Monopile foundations are by far the most widely used method to support offshore wind turbines due to their simplicity and low cost [2]. These monopiles are often subjected to non-linear wave loads since they are always located in shallow seas with a maximum depth of 50 m. To achieve cost reduction and optimal design, the industry is pursuing a complete understanding of the non-linear wave loads on monopile foundations [3]. There are many kinds of research on monopile foundation, such as the scour around the monopile [4–6], monopile-solid interaction [7], hybrid monopile foundation [8,9], and hydrodynamic characteristics of monopile [10–13].

For hydrodynamic calculation, much linear potential theory forms the basis of most commercial software. At present, the software widely used in hydrodynamic engineering calculations are FAST<sup>©</sup> [14], SESAM<sup>™</sup> [15], AQWA<sup>™</sup> [16], and WAMIT<sup>™</sup> [17]. The

hydrodynamic calculations in Fast© are based on the WAMIT™. The frequency domain calculation function of the above software programs is based on linear potential flow. There exists a large body of research already published on hydrodynamic flows around a cylinder using the linear potential flow theory. MacCamy and Fuchs [18] published an analytic solution of wave diffraction from monopiles based on linear potential theory. They considered a bottom-mounted vertical cylinder subjected to regular wave loading in the water of unlimited and arbitrary depth. However, linear diffraction theory is insufficient for predicting wave run-up accurately when waves are highly non-linear. By comparing experimental results with diffraction theory solutions, Thomas [19] concluded that irregular wave run-up on vertical monopile can be accurately predicted using long wave theory. He conducted large-scale experiments focusing on the near-breaking and breaking waves. Niedzwecki et al. [20] performed small-scale experiments to investigate wave run-up on vertical cylinders and proved that the linear assumption can significantly under-predict the crest elevation around cylinders in steep wave conditions.

In search of more accurate calculation methods, there are many studies about non-linear forces on monopile. It is found experimentally that the contribution of non-linear high-frequency force is up to 10–20% of the total wave-induced load [21]. According to Tromans et al. [22], there is a strong correlation between the high-frequency forces and wave scattering, using the regular and the irregular wave action on a vertical cylinder. High-frequency wave force could oscillate at a magnitude as large as 20% of the linear component of the wave load. Chen et al. [23] experimentally extracted the higher harmonics in wave–structure interactions using focused wave groups. For strongly non-linear wave conditions, the linear component is less than 40% of the total wave load, and the high-order harmonics contribute more than 60% of the wave loading, signifying the importance of studying high-order non-linear wave loading on offshore structures. Kristiansen and Faltinsen [24] found that the predicted third harmonic loads based on potential theory are shown to agree well with the experiments for small to medium wave steep, up to a rather distinct limiting wave steepness, under the non-breaking wave conditions. Furthermore, the local Keulegan–Carpenter (KC) number indicates that flow separation will occur for the wave conditions where there are discrepancies between experimental and numerical results. The proportion of high-order wave force is too large to be ignored. However, it can be seen that the calculated results of potential flow could be different from the experiment due to flow separation even under the non-breaking wave.

Some research about the non-linear run-up around the monopile was conducted as well. Stansberg et al. [25] observed significant non-linear effects, especially in steep waves, with the maximum elevation in front of the column increases. Swan et al. [26] highlighted the importance of non-linear wave scattering from a slender vertical surface piercing column and also investigated the non-linear, higher-harmonic wave loading experimentally, and characterized high-frequency wave scattering around the cylinder. They also explained why low-order diffraction solutions are inappropriate. Stansberg et al. [27] remarked that non-linear tools based on potential theory have some limitations due to model wave-breaking and viscous effects in simulating non-linear wave–body interaction flows. LD Vos et al. [28] present a physical model study on the run-up characteristics of offshore wind turbine foundations under the influence of regular and irregular waves, finding that the position with the lowest run-up level is located under  $135^\circ$ , while the run-up at that position amounts to approximately 40% to 50% of the maximum run-up. Kriebel [29,30] reported that the measured run-up values and the second-order theory exceed the linear prediction by over 50% in some cases. Furthermore, the study found that the non-linear diffraction theory is valid for the same relative depth and wave steepness conditions as the Stokes 2nd-order plane-wave theory. Andersen [31] et al. conducted a physical model to investigate wave run-up on cylindrical piles under different ratios of diameter to water depth and wave heights to water depth for regular and irregular waves. The study revealed poor agreement between the measured run-up values and both linear and second-order diffraction solutions, particularly in steep incident waves. They also

noted that the poor agreement is due to the effects of wave breaking and viscosity. These studies primarily concentrate on analyzing individual points of wave run-up rather than considering the complete distribution of wave run-up around the monopile or the energy transfer relationship between the fundamental and higher harmonic components.

There are many modeling techniques and calculation methods employed to understand the associated problems with wave loading on monopiles, such as the Morison equation, potential flow theory, and the computational fluid dynamics (CFD) method, etc. The Morison equation [32] is applied to determine the linear component of wave loading. However, in strongly non-linear waves or large-scale structure conditions, the Morison equation method underestimates the peak forces on a fixed cylinder [12]. CFD approaches can simulate strongly non-linear free-surface flow for accessible, detailed information about various flow features. However, the CFD method is computationally expensive and time-consuming for high-fidelity solutions. Hence, it is not widely used in commercial simulations. The potential theory is more commonly adopted in commercial simulations due to its comparatively fast and accurate characteristics. Chen et al. [23] display the variation of extracted harmonics wave force on monopile with the wave steepness, which shows that the 3rd- and 4th-order wave forces can be less than that of the 2nd-order component with one order of magnitude. Ning et al. [33] conducted several numerical simulations based on diffraction theory and experiments to model focused wave run-up and the non-linear interaction with a vertical fixed cylinder. Compared with the 1st-, 2nd-order, and fully non-linear solutions, the 2nd-order solutions are very close to the fully non-linear solutions. It can be concluded that the 2nd-order non-linear potential theory can get considerable precision at a lower cost. However, the coefficient matrix must be updated, and the grid must be rebuilt at every time step in the fully non-linear potential model, requiring significant computing resources. When it comes to strongly non-linear conditions, the grid is prone to distortion, which may lead to non-convergence of the solution. Moreover, grid construction relies heavily on the users' experience to generate accurate results. Therefore, the 2nd-order non-linear method is adopted in the present work.

The review of research on wave loads and run-ups on vertical cylinders shows that the linear method using simple approaches based on potential-flow theory cannot provide accurate solutions. While dealing with the subject of steeper conditions, a higher-order potential-flow-based approach can yield a more precise fit result. However, in extreme non-breaking wave cases, the potential theory will over-predict the higher harmonic response, and the discrepancy generally increases monotonically with increasing wave steepness, as discussed in [24]. It is argued that viscous flow separation or viscous effects cause these significant discrepancies [24]. However, there is no such clear limitation indicating the range of potential flow capability of monopile simulation under non-breaking wave conditions.

The potential theory is widely used in commercial applications to enable numerical simulations to be conducted at affordable costs. The purpose of this paper is to study the non-linear hydrodynamic features on the monopile foundation in the lab conditions and distinguish the capability of non-linear potential theory to guide commercial simulation. The structure of the paper is as follows: In Section 2, the experimental setup for the monopile study is introduced. The model for the wave-monopile interaction is established in Section 3. The responses of the monopile under regular wave conditions are investigated in Section 4. Section 5 discusses the harmonic structure observed on the monopile. Finally, in Section 6, the major findings are concluded.

## 2. Experiments

Figure 1 shows a photo of the experimental setup of a 1:30 scale monopile foundation model in the 62.5 m long, 2 m wide, and 1.2 m high experimental wave flume at the State Key Laboratory of Coastal and Offshore Engineering in Dalian University of Technology, China. The wave maker can generate unidirectional waves with a frequency range of  $0.2 \text{ Hz} \leq f \leq 2 \text{ Hz}$  and amplitudes in the range of  $0.03 \text{ m} \leq A \leq 0.5 \text{ m}$ . The monopile model with a diameter ( $D$ ) of 0.3 m is installed at 32.5 m downstream of the wave paddles and

the center of the flume width, as shown in Figure 2. Since  $B/D \geq 5$ , the influence of the lateral flume walls is negligibly weak, as discussed by Soares [34], where  $B$  is the width of the flume. The static water depth  $h$  is 0.8 m.



Figure 1. Photograph of the model monopile.

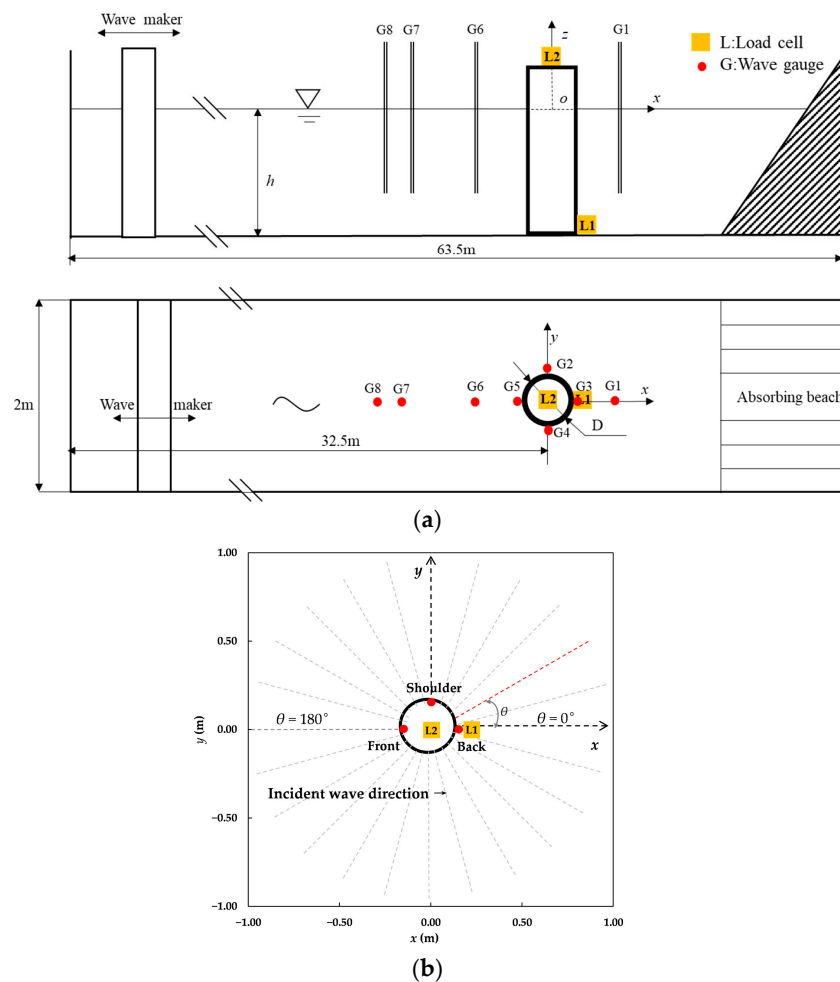


Figure 2. Sketch of the experimental setup: (a) global setting and (b) detail setting around the monopile.

A Cartesian coordinate system “ $O(xyz)$ ” is defined with its origin at the center of the monopile on the static water surface with  $x$  in the wave propagation direction and  $z$  in the upward direction. The top and bottom surfaces of the model are rigidly connected with the stiff frames supporting the monopile using two load cells (labeled as L1 and L2 in Figure 2), i.e., L1 (0.0 m, 0.00 m, 0.50 m) and L2 (0.15 m, 0.00 m, −0.80 m). Two fixed joint supports are imposed at the top and back of the monopile, respectively. However, it is noted that there is a 1 mm gap between the cylinder base and the wave flume floor. The load cells are used to record the wave force on the model at a sampling rate of 1000 Hz. Eight wave gauges, i.e., G1–G8, as shown in Figure 2a, are used to record surface elevations around the monopile at a sampling rate of 100 Hz. In Figure 2b, a polar coordinate system ( $r, \theta$ ) is defined in which  $r = 0$  corresponds to the monopile center and  $\theta = 0^\circ$  is the wave propagation direction. Wave gauges G2–G5 are positioned within 10 mm of the surface of the monopile ( $0.15 \text{ m} \leq r \leq 0.151 \text{ m}$ ) for accurate run-up detection [23]. The positions of the wave gauges are listed in Table 1.

**Table 1.** Position of the wave gauges.

		Position (m)							
		G1	G2	G3	G4	G5	G6	G7	G8
$x$		1.5	0	−0.15	0	0.15	−1.65	−4.15	−4.65
$y$		0	0.15	0	−0.15	0	0	0	0

Strongly non-linear regular but non-breaking waves [35] are generated in the wave flume. To investigate the influence of wave non-linearity, five wave amplitudes  $A$  and eight wave periods  $T$  for each amplitude, totaling 40 cases, are studied, as listed in Table 2. Such wave characteristics are measured at 32.5 m downstream of the wave paddles in the middle of the flume width, where the central axis of monopile sets. The other non-linear parameter usually used in the study is the ratio of wave height to wavelength  $\varepsilon = kA/\pi$ . In the finite amplitude wave (Stokes) theory, there is a limit  $\varepsilon_{lim}$  without structure. The limit ratio is about 0.142. When the wave steepness is greater than  $\varepsilon_{lim}$ , the wave breaks. When a structure interacts with waves, the waves will break at a ratio smaller than  $\varepsilon_{lim}$ , which depends on the scale of the structure.

**Table 2.** Tested wave conditions.

$T$ (s)	$kA$	$A$ (m)	1.00	1.15	1.30	1.45	1.60	1.75	1.90	2.05
0.0250	0.101	0.077	0.062	0.052	0.044	0.039	0.035	0.031		
0.0375	0.151	0.116	0.093	0.077	0.066	0.058	0.052	0.047		
0.0500	0.202	0.154	0.124	0.103	0.088	0.078	0.069	0.063		
0.0625	0.252	0.193	0.155	0.129	0.111	0.097	0.087	0.078		
0.0750	0.303	0.232	0.186	0.155	0.133	0.117	0.104	0.094		

### 3. Numerical Methodology

The higher-order boundary element method (HOBEM) based on potential-flow theory is employed to investigate the hydrodynamic flow field around the monopile. A Cartesian coordinate system “ $O(xyz)$ ” is defined as similar to the experimental model shown in Figure 2. Figure 3a shows the numerical setup of the hydrodynamic model in the monopile. In the figure,  $S_f$  is the mean free surface,  $S_D$  the solid surface of the monopile, and  $S_B$  the surface of the flume bottom.

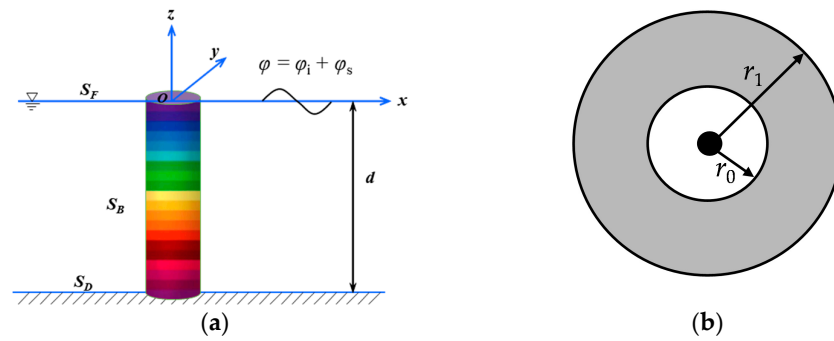


Figure 3. Definition sketch of (a) coordinate systems and simulation domain and (b) the sponge layer.

It is assumed that the fluid is incompressible and inviscid. The wave field around the monopile foundation can be described by a complex spatial potential  $\varphi(x, y, z, t)$ . Following the incident and scattering potential separation technique, the spatial potential  $\varphi$  can be divided into a known incident potential  $\varphi_i$  and an unknown scattering potential  $\varphi_s$  [36]. The scattered potential satisfies the following governing equation:

$$\nabla \varphi_s^{(m)}(x, y, z, t) = 0, \tag{1}$$

where the superscript  $m$  (1 or 2) denotes the order of the perturbation expansion, the corresponding boundary and initial conditions for all scattered potential can be described as follows:

$$\frac{\partial \eta_s^{(m)}}{\partial t} = \frac{\varphi_s^{(m)}}{\partial z} - v_{(r)} \eta_s^{(m)} - f_m' \quad (m = 1 \ \& \ 2), \text{ on } S_F \tag{2}$$

$$\frac{\partial \phi_s^{(m)}}{\partial t} + g \eta_s^{(m)} + v_{(r)} \phi_s^{(m)} - f_m' = \begin{cases} \frac{\partial \phi_s^{(1)}}{\partial n} \quad (m = 1) \\ \eta_s^{(1)} \frac{\partial \phi_s^{(1)}}{\partial n} + \frac{\partial \phi_s^{(2)}}{\partial n} \quad (m = 2) \end{cases}, \text{ on } S_F \tag{3}$$

$$\frac{\partial \phi_s^{(m)}}{\partial n} = -\frac{\partial \phi_i^{(m)}}{\partial n} \quad (m = 1 \ \& \ 2), \text{ on } S_D \text{ and } S_B \tag{4}$$

$$\phi_s^{(m)} = 0 \ \& \ \eta_s^{(m)} = 0 \quad (m = 1 \ \& \ 2), \text{ when } t = 0 \tag{5}$$

$$\lim_{x \rightarrow \infty} \nabla \phi \rightarrow 0 \quad (m = 1 \ \& \ 2) \tag{6}$$

where  $\frac{\partial}{\partial n}$  denotes the normal derivative on the solid surface,  $\eta_s$  denotes the scattered wave elevation,  $f_m'$  and  $f_m''$  are the forcing terms on the free surface [37].

As the numerical domain is limited, a damping layer was set to avoid the reflection of scattered waves from the outer boundary, as shown in Figure 3b, which can make the numerical simulation perform similarly to the actual open sea. A damping coefficient  $v_{(r)}$  is included in the free surface dynamic boundary condition in the damping layer [37]. The damping coefficient is calculated according to:

$$v(r) = \begin{cases} \alpha_0 \omega \left( \frac{r-r_0}{\beta_0 \lambda} \right)^2 & r_0 \leq r \leq r_1 = r_0 + \beta_0 \lambda \\ 0 & r < r_0 \end{cases} \tag{7}$$

where  $\lambda$  is the wavelength, and the outer and inner boundaries of the damping layer are  $r_1$  and  $r_0$ , respectively, as shown in Figure 3. Green's second identity can be applied to the above boundary value problem with the Rankine source and its image of the seabed as the Green function [38].

$$G(p_s, q_f) = -\frac{1}{4\pi} \left( \frac{1}{R_0} + \frac{1}{R_z} \right) \tag{8}$$

where  $p_s = (x_1, y_1, z_1)$  and  $q_f = (x, y, z)$  are the source point and the field point, respectively, and

$$R_0 = \sqrt{(x-x_1)^2 + (y-y_1)^2 + (z-z_1)^2} \tag{9}$$

$$R_z = \sqrt{(x-x_1)^2 + (y-y_1)^2 + (z+z_1+2h)^2} \tag{10}$$

Then, the integral equation for the scattered wave can be obtained:

$$\alpha \varphi_s^{(m)}(p_s) = \iint_S \left[ \varphi_s^{(m)}(q_f) \frac{\partial G(q_f, p_s)}{\partial n} - G(q_f, p_s) \frac{\partial \varphi_s^{(m)}(q_f)}{\partial n} \right] dS \tag{11}$$

where the boundary surface  $S$  includes the mean free surface ( $S_F$ ) [36] and the solid surface ( $S_D$ ),  $\alpha$  is the solid angle coefficient. In the time domain, the fourth-order Adams–Bashforth predictor-corrector method is applied to predict the free surface and potential. The detailed procedure can be found in [37]. Wave forces  $F$  on the monopile are calculated by integrating the pressure over the wetted surface of the monopile:

$$F = \iint_{S_{\text{monopile}}} p n dS \tag{12}$$

where  $n = (n_x, n_y, n_z)$ ,  $F = (F_x, F_y, F_z)$ , “ $S_{\text{monopile}}$ ” denotes the wet surface of the monopile.

#### 4. Results and Discussion

##### 4.1. Comparisons between the Numerical and Experimental Results

The geometry of the numerical model setup is identical to the experiment shown in Figure 1. The damping layer extends from  $r_0 < r < r_1$  in Figure 4a. Based on the previously published work [38], the outer and inner boundaries of the damping layer are  $r_1 = 2\lambda$  and  $r_0 = \lambda$ , respectively. The  $x$ - and  $y$ -axis symmetry is used in the present model to reduce the number of elements in the calculation process. Meanwhile, three sets of grids with different sizes are selected to verify the convergence. In grid 1, the numbers of the computational elements on the monopile surfaces and free surfaces are 84 and 867, respectively. In grid 2, the numbers of the computational elements on the monopile surfaces and free surfaces are 127 and 1244, respectively. In grid 3, the numbers of the computational elements on the monopile surfaces and free surfaces are 145 and 1448, respectively. After the mesh convergence test, grid 2 is applied in simulation with quad elements. The mean size of elements on the monopile surfaces and free surfaces in grid 2 are 0.04 and 0.003, respectively. The time step is specified to be  $T/100$ .

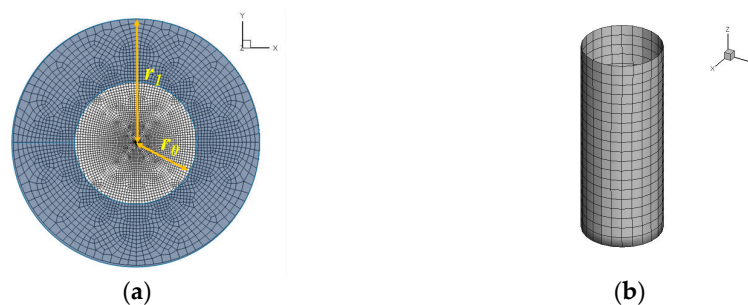


**Figure 4.** (a) Mesh on the free surface of the simulation domain and (b) mesh on the surface of the monopile body.

Two typical steep waves are selected for the numerical and experimental results comparison: Case 1 ( $A = 0.025$  m,  $T = 1.45$ s,  $kA = 0.052$ ) and Case 2 ( $A = 0.0750$  m,  $T$

= 2.05 s,  $kA = 0.094$ ). Figure 5 shows the comparison of the normalized time histories of the wave elevation at three wave probes located at the front ( $\eta_{180^\circ}$ ), shoulder ( $\eta_{90^\circ}$ ), and back ( $\eta_{0^\circ}$ ) points on the monopile, respectively, and the horizontal wave force. The wave elevation  $\eta$  is normalized by the incident wave amplitude ( $A$ ), and the time ( $t$ ) is normalized by the wave period ( $T$ ). The wave force is normalized by  $\rho gAR^2$ , where  $\rho$  and  $g$  are the water density and gravity acceleration, respectively. The linear and 2nd-order non-linear results both agree well with the experimental results in Case 1. In Case 2, the non-linearity of the waves increased significantly, leading to a noticeable discrepancy between the linear results and the experimental results. Nevertheless, the non-linear results demonstrated good agreement with the experimental results. In summary, the present non-linear numerical results are in close agreement with the experiments, verifying the validity of the present model.

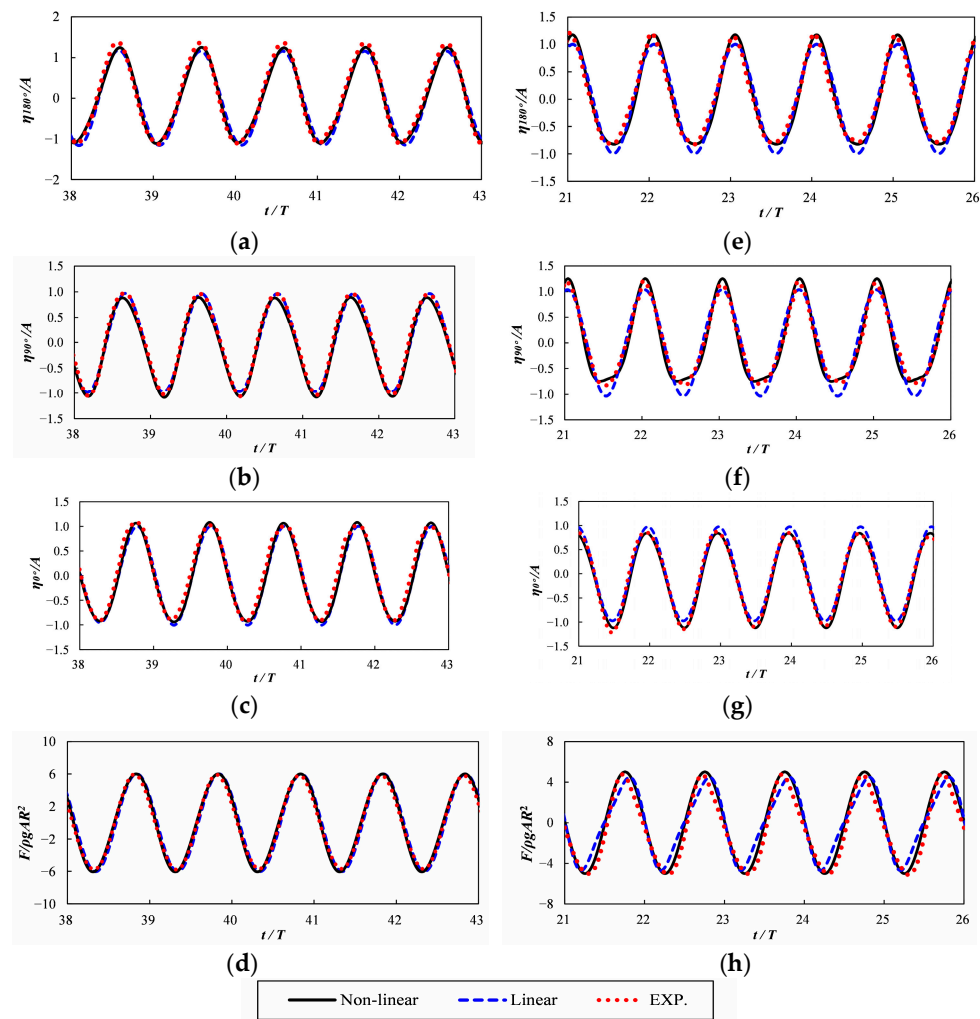


**Figure 5.** Time series of the simulated and measured run-up around the monopile and wave load on the monopile: (a) run-up at the front point in Case 1, (b) run-up at the shoulder point in Case 1, (c) run-up at the back point in Case 1, (d) horizontal wave load in Case 1, (e) run-up at the front point in Case 2, (f) run-up at the shoulder point in Case 2, (g) run-up at the back point in Case 2, and (h) horizontal wave load in Case 2.

#### 4.2. Wave Load on the Monopile

The amplitude of wave force obtained using the linear and non-linear potential theory models is compared with the experimental data in Figure 6. The amplitude of the wave force  $F_{total}$  is the average amplitude of the wave force over three consecutive periods in a stable state. At the same amplitude  $A$ ,  $F_{total}$  increases initially and then decreases

with the increase of  $kA$ . As  $kA$  increases above 0.15, the non-linear potential theory wave load magnitudes diverge from the experimental data. Under strongly non-linear wave conditions, the numerical results based on potential flow theory could overpredict the actual loads to a certain degree due to viscous effects. This phenomenon was well documented and explained by Kristiansen and Faltinsen [24]. As wave slope  $kA > 0.15$ , the  $KC$  number is greater than 3.5 in the present work, where fluid separation may appear and cause significant discrepancies between experimental data and numerical results [24]. In the range of wave steep  $kA < 0.15$ , a good agreement between the 2nd-order non-linear hydrodynamic loads and the experimental data has been achieved, as shown in Figure 6. This illustrates that the non-linear potential theory works well in the range of  $kA < 0.15$ .

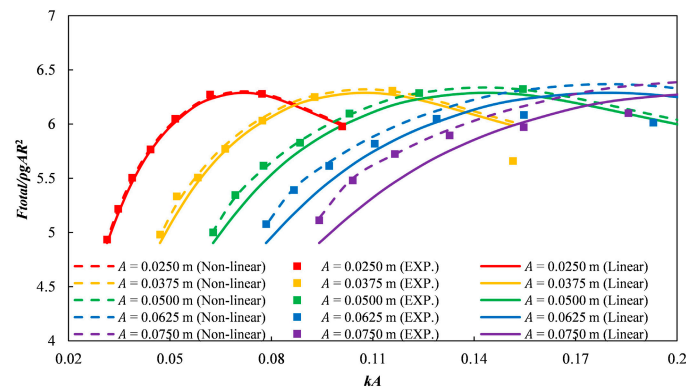
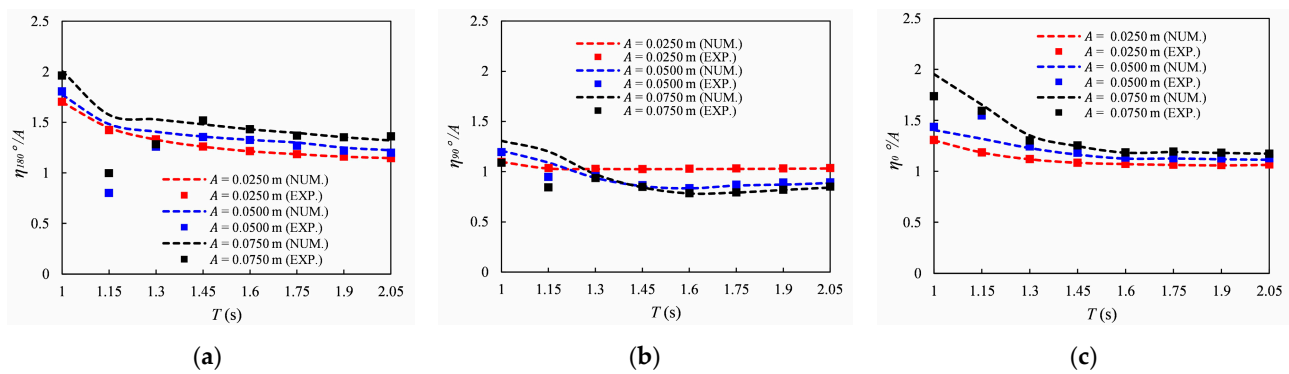


Figure 6. Wave force on monopile for different wave steepness.

#### 4.3. Run-Up on the Monopile

Figure 7 displays the variation in run-up at the front, shoulder, and back points of the monopile. In the range of  $1.00 \leq T \leq 2.05$ , numerical results of maximum wave run-up on the monopile for  $A = 0.025$  m,  $A = 0.050$  m, and  $A = 0.075$  m cases are generally in good agreement with experimental data. Nevertheless, resonance effects occur in the flume–transverse direction at  $T = 1.15$  s condition when the wavelength is 2.0355 m close to the flume width of 2 m, effectuating exceptional run-up conditions (Figure 8) observed in the experiment. The transverse resonance increases the run-up at the back of the monopile and reduces the run-up at the front of the monopile, as shown in Figure 9, resulting in the discrepancy between experimental data and the numerical analysis. However, in the actual sea state, there is no effect of the flume side wall. Such resonance seriously affects the results of the experimental data, which may be misleading. According to Figure 7, the dimensionless run-up on the front and back of the cylinder decreases as  $T$  increases under the same wave amplitude conditions. The dimensionless run-up at the shoulder of the cylinder initially decreases and then increases as  $T$  increases. Additionally, the non-dimensional run-up on the front and back of the cylinder increases as  $A$  increases. As the wave period increases, the variations of all the run-ups decrease and tend toward stable values. This is because the wavelength increases in long-period wave circumstances, the transmission capacity of the wave is enhanced, the reflection decreases, and the run-ups tend to saturation. To investigate the maximum circumferential run-up around the monopile, Figure 10 displays the maximum run-up for selected wave periods and different values of  $\theta$ . The maximum run-up function on  $\theta$  presents a W-shape. The run-up peak value appears at the incident wave side ( $\theta = 180^\circ$ ) for each wave condition due to full reflection, especially for the smaller wave period. The two symmetrical minima points lie in the zone of ( $45^\circ \leq \theta \leq 90^\circ$ ) and ( $270^\circ \leq \theta \leq 315^\circ$ ), whose position shifts towards the positive direction of the  $x$ -axis with the increase of wave non-linearity.



**Figure 7.** The run-up on monopile for different wave steepness: (a) run-up at the front point, (b) run-up at the shoulder point, and (c) run-up at the back point.

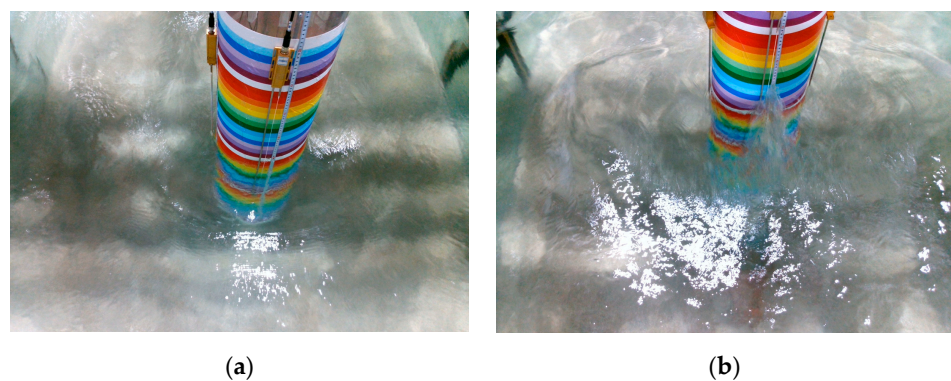


**Figure 8.** Transverse wave resonance phenomenon: (a) front view; (b) back view ( $T = 1.15$  s,  $A = 0.075$  m).

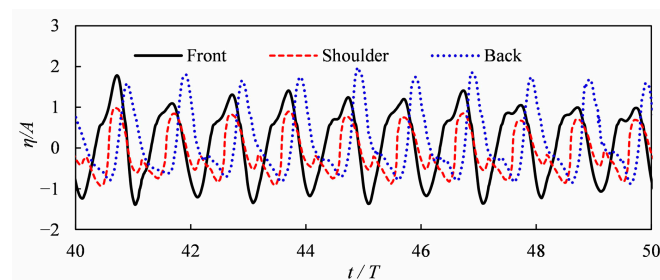


**Figure 9.** The measured free surface elevation time histories (front, shoulder, and back) under wave conditions of ( $T = 1.15$  s,  $A = 0.075$  m).

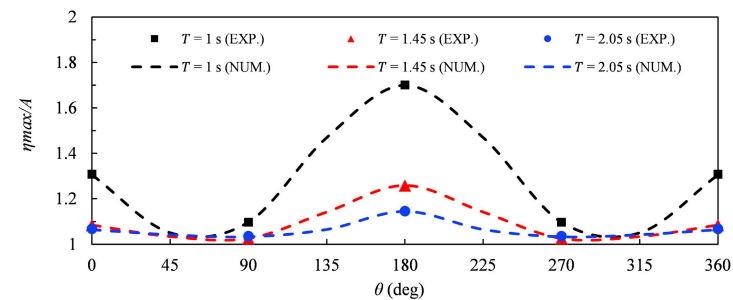


**Figure 10.** Normalized maximum run-up around the monopile.

## 5. Harmonic Structure on Monopile

### 5.1. Harmonic Wave Load Component

Figure 11 shows a  $kh$ - $A$  plot depicting the numerical proportions of first-order and second-order wave loads in the total wave load. The time history of second-order wave force can be obtained by the means that the linear result is subtracted from the non-linear result. For a constant  $kh$  the contribution of the second-order wave load increases with the increase of  $A/h$ . For a constant  $A/h$ , the contribution of the second-order wave load increases initially and then decreases with the increase of  $kh$ . The contribution of first-order wave height meets the minimum value, and the contribution of second-order wave load meets the maximum value where  $kh$  is 1.11 for every amplitude. This indicates that there exists a certain governing wave number  $kh$  where the proportion of non-linear wave load component reaches the maximum, regardless of what value  $A/h$  is. At a constant proportion of first-order to second-order components (e.g., the dashed line in Figure 11), as  $kh$  increases, the wave amplitude decreases at first, then increases before slightly decreasing.

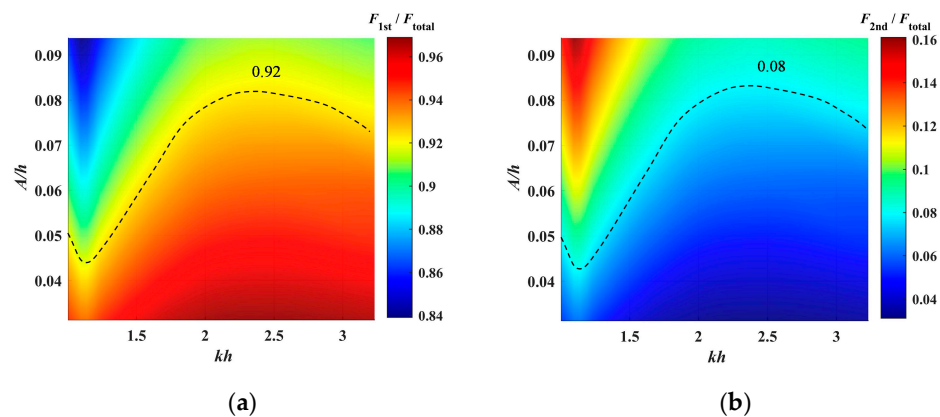


**Figure 11.** Variation of harmonics with the wave steepness  $kh$ : (a) linear force component; (b) second-harmonic forces.

### 5.2. Harmonics of Wave Run-Up Component

Figure 12 shows the variation of measured harmonics run-up components with the wave steepness  $kA$ , with the fitting curve utilizing the least square method in every subplot. Although the data in Figure 12b is not very concentrated, there is a clear trend comparatively that the dimensionless run-ups decrease first and then decrease. The incident waves propagate in the positive  $x$ -direction over a flatbed, passing the front, shoulder, and back points. As the waves pass the monopile, their non-linearity increases. It can be seen that in Figure 12a,d,g, the corresponding first-order run-up component decreases according to the wave passing sequence. The composition of the second-order component increases when it interacts with the monopile, at the incident wave side increasing first and then decreasing; at the shoulder, the second harmonic component increases roughly linearly, and at the back, it exhibits quadratic growth. The third-order wave force component presents the same trend as the second-order harmonic component. The third-order run-up at the back side is larger than that at the front side. This indicates that the high-order component of run-up varies with the position on the surface of the monopile, and the non-linear component of run-up is the largest at the lee side of the structure. Energy transfer from the fundamental component to the higher-order components was also observed and is most apparent on the backward side. In addition, the linear component of run-up only accounts for 60% of the elevation, while the non-linear run-up component accounts for up to 40%. This indicates that the linear results alone significantly underestimate run-up.

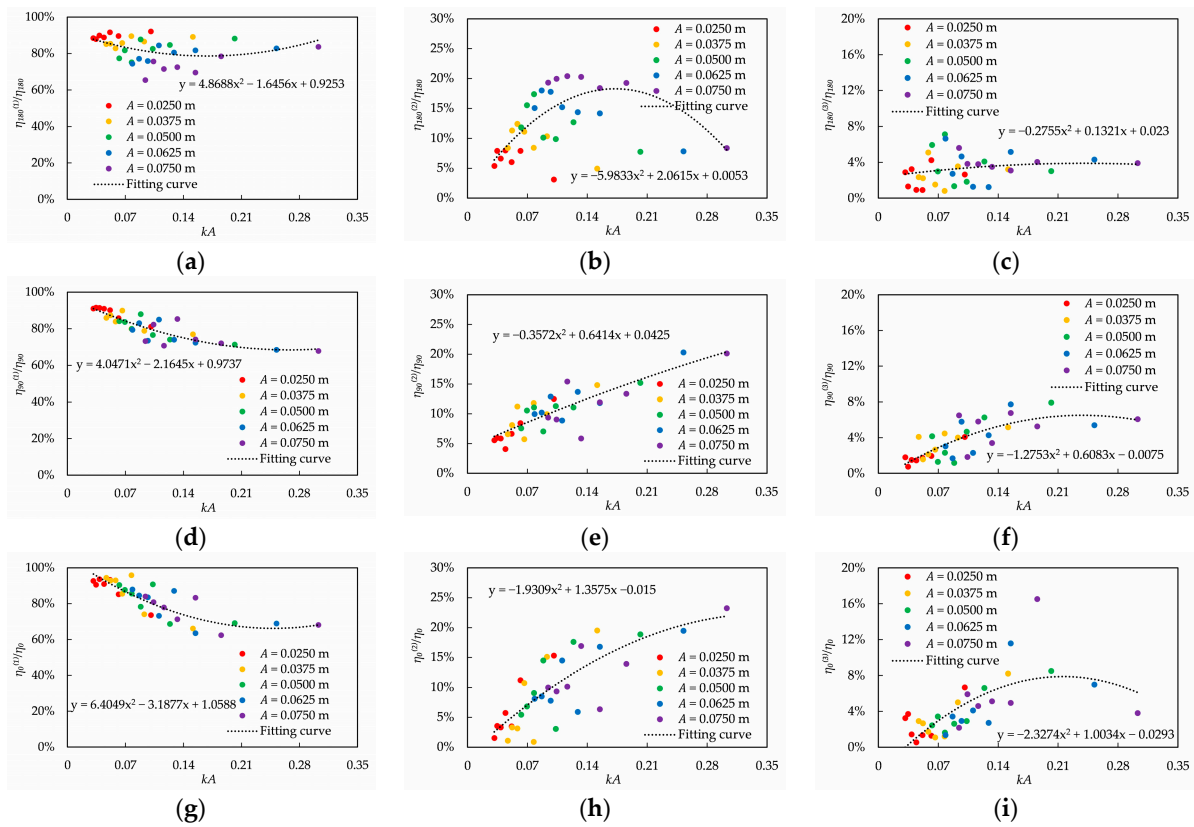


**Figure 12.** Variation of measured harmonics with the wave steepness  $kA$ : (a) linear component on front point, (b) second-harmonic component on front point, (c) third-harmonic component on front point, (d) linear component on shoulder point, (e) second-harmonic component on shoulder point, (f) third-harmonic component on shoulder point, (g) linear component on back point, (h) second-harmonic component on back point, and (i) third-harmonic on back point.

## 6. Concluding Remarks and Future Works

### 6.1. Concluding Remarks

Both the physical experiment and numerical investigation are employed to investigate the non-linear characteristics of the wave loads and run-up on an offshore wind turbine monopile foundation under regular waves. The major conclusions are summarized as follows.

Within the range of wave slope  $kA < 0.15$ , the 2nd-order non-linear potential theory is acceptable for the simulation of monopile response. In this region, this method can provide a fast and low-cost simulation. The wave loads resulting from different incident wave amplitudes  $F_{total}$  exhibit a similar trend with the increase of  $kA$ , i.e., the wave force increases at first and then decreases. Under the same wave period conditions, the dimensionless wave force increases slightly as the amplitude  $A$  increases.

The maximum run-up function on the coordinate angle  $\theta$  presents a W-shape, with a maxima point appearing on the frontward side ( $\theta = 180^\circ$ ) on account of the full reflection. The positions of two symmetrical minima points vary in the regions of ( $45^\circ \leq \theta \leq 90^\circ$ ) and ( $270^\circ \leq \theta \leq 315^\circ$ ), according to the wave non-linearity.

Energy transfer from the fundamental wave component to higher-order components is observed, particularly at the backward side of the monopile. For certain wave cases, the linear run-up component was less than 60%, which indicates that the linear results severely underestimated the run-up.

In addition, transverse resonance occurred in the flume due to the wavelength corresponding to the flume width, inducing wave run-up at the backward position, with the run-up larger at the leeward side of the monopile than at the weather side.

## 6.2. Future Works

Current research does not consider the impact of wave breaking, the higher-order non-linear effect (more than second-order), and the viscous effects. Subsequent studies should incorporate a more comprehensive method to study the nonconforming portion.

The calculation and analysis of the overall hydrodynamic response of a monopile do not consider the wind conditions. In future work, additional calculation modules, including wind, sea ice, and earthquake loads, may be added to the numerical model.

Furthermore, the experiment reveals the peculiar occurrence of flume transverse resonance, which is not explicable due to the constraints of the calculation theory.

**Author Contributions:** Conceptualization, S.D. and D.N.; methodology, S.D. and D.N.; S.D.; validation, S.D.; formal analysis, S.D.; investigation, S.D.; resources, S.D.; data curation, S.D.; writing—original draft preparation, S.D.; writing—review and editing, D.N., M.Q., L.L., S.W. and C.Z.; visualization, S.D.; supervision, D.N. All authors have read and agreed to the published version of the manuscript.

**Funding:** This work is supported by the National Natural Science Foundation of China (Grant Nos. 52011530183), LiaoNing Revitalization Talents Program (Grant No. XLYC2002033), Research Fund of China Three Gorges Group Co., Ltd. (201166740004) and the Fundamental Research Funds for the Central Universities (DUT21LAB116).

**Institutional Review Board Statement:** Not applicable.

**Informed Consent Statement:** Not applicable.

**Data Availability Statement:** Not applicable.

**Conflicts of Interest:** The authors declare no conflict of interest.

## References

1. International Energy Agency. *Offshore Wind Outlook 2021. World Energy Outlook Special Report*; International Energy Agency: Paris, France, 2022.
2. Butterfield, S.; Musial, W.; Jonkman, J.; Sclavounos, P. Engineering Challenges for Floating Offshore Wind Turbines. In Proceedings of the 2005 Copenhagen Offshore Wind Conference, Copenhagen, Denmark, 26–28 October 2005.
3. Gao, Z.; Bingham, H.; Nicolls-Lee, R.; Adam, F.; Ren, H. Proceedings of the Offshore Renewable Energy, 19th ISSC Congress, Cascais, Portugal, 7–10 September 2015.
4. Corvaro, S.; Marini, F.; Mancinelli, A.; Lorenzoni, C.; Brocchini, M. Hydro- and Morpho-dynamics Induced by a Vertical Slender Pile under Regular and Random Waves. *J. Waterw. Port Coast. Ocean. Eng.* **2018**, *144*, 04018018. [[CrossRef](#)]
5. Corvaro, S.; Crivellini, A.; Marini, F.; Cimarelli, A.; Capitanelli, L.; Mancinelli, A. Experimental and numerical analysis of the hydrodynamics around a vertical cylinder in waves. *J. Mar. Sci. Eng.* **2019**, *7*, 453. [[CrossRef](#)]
6. Sumer, B.M.; Fredse, J. The mechanics of scour in the marine environment. In *Advanced Series on Ocean Engineering*; World Scientific: Singapore, 2002; Volume 17.
7. Abhinav, K.; Saha, N. Dynamic analysis of monopile supported offshore wind turbines. *Geotech. Eng.* **2017**, *170*, 428–444. [[CrossRef](#)]
8. Ma, H.; Yang, J. A novel hybrid monopile foundation for offshore wind turbines. *Ocean. Eng.* **2020**, *198*, 106963. [[CrossRef](#)]
9. Zhou, Y.; Ning, D.; Shi, W. Hydrodynamic investigation on an OWC wave energy converter integrated into an OWT monopile. *Coast. Eng.* **2020**, *162*, 103731. [[CrossRef](#)]
10. Zeng, X.; Shi, W.; Michailides, C.; Zhang, S.; Li, X. Numerical and experimental investigation of breaking wave forces on a monopile-type offshore wind turbine. *Renew. Energy* **2021**, *175*, 501–519. [[CrossRef](#)]
11. Grue, J.; Bjorshol, G.; Strand, O. Nonlinear wave loads which may generate ‘ringing’ responses of offshore structures. In Proceedings of the International Workshop on Water Waves and Floating Bodies, Osaka, Japan, 17–20 April 1994.
12. Chaplin, J.R.; Rainey, R.C.T.; Yemm, R.W. Ringing of a vertical cylinder in waves. *J. Fluid Mech.* **1900**, *350*, 119–147. [[CrossRef](#)]
13. Huseby, M.; Grue, J. An experimental investigation of higher-harmonic wave forces on a vertical cylinder. *J. Fluid Mech.* **2000**, *414*, 75–103. [[CrossRef](#)]
14. Lee, C. *WAMIT Theory Manual*; Massachusetts Institute of Technology, Department of Ocean Engineering: Cambridge, MA, USA, 1995.
15. DNV, G.L. *SESAM User Manual*; WADAM: Høvik, Norway, 2019.
16. ANSYS. *AQWA Theory Manual*; ANSYS: Canonsburg, PA, USA, 2013.
17. Jonkman, J.M.; Buhl, M.L. *FAST User’s Guide*; National Renewable Energy: Salt Lake City, UT, USA, 2005.
18. MacCamy, R.C.; Fuchs, R.A. Wave forces on piles: A diffraction theory. Beach Erosion board office of the chief engineers, department of the army. *Tech. Memo.* **1954**, *69*, 1–17.

19. Morris-Thomas, M.T.; Thiagarajan, K.P. The run up on a cylinder in progressive surface gravity waves: Harmonic components. *Appl. Ocean Res.* **2004**, *26*, 98–113. [[CrossRef](#)]
20. Niedzwecki, J.M.; Duggal, A.S. Wave run-up and forces on cylinders in regular and random waves. *J. Waterw. Port Coast. Ocean. Eng.* **1992**, *118*, 615–634. [[CrossRef](#)]
21. Malenica, S.; Molin, B. Third-harmonic wave diffraction by a vertical cylinder. *J. Fluid Mech.* **1995**, *302*, 203–229. [[CrossRef](#)]
22. Tromans, P.; Swan, C.; Masterton, S. *Nonlinear Potential Flow Forcing: The Ringing of Concrete Gravity-Based Structures*; Health and Safety Executive: Bootle, UK, 2006; pp. 4–68.
23. Chen, L.; Zang, J.; Taylor, P.H.; Sun, L.; Morgan, G.; Grice, J.; Orszaghova, J.; Ruiz, M.T. An experimental decomposition of nonlinear forces on a surface-piercing column: Stokes-type expansions of the force harmonics. *J. Fluid Mech.* **2018**, *848*, 42–77. [[CrossRef](#)]
24. Kristiansen, T.; Faltinsen, O.M. Higher harmonic wave loads on a vertical cylinder in finite water depth. *J. Fluid Mech.* **2017**, *833*, 773–805. [[CrossRef](#)]
25. Stansberg, C.T.; Nielsen, F.G. Nonlinear wave—Structure interaction on floating production systems. In Proceedings of the 11th ISOPE Conference IV, Stavanger, Norway, 17–22 June 2001.
26. Swan, C.; Masterton, S.; Sheikh, R.; Cavalletti, A. Wave forcing and wave scattering from a vertical surface-piercing cylinder. In Proceedings of the 24th OMAE Conference, Halkidiki, Greece, 12–17 June 2005.
27. Stansberg, C.T.; Kristiansen, T. Non-linear scattering of steep surface waves around vertical columns. *Appl. Ocean Res.* **2005**, *27*, 65–80. [[CrossRef](#)]
28. De Vos, L.; Frigaard, P.; De Rouck, J. Wave run-up on cylindrical and cone shaped foundations for offshore wind turbines. *Coast. Eng.* **2007**, *54*, 17–29. [[CrossRef](#)]
29. Kriebel, D. Non-linear wave interaction with a vertical circular cylinder. Part II: Wave run-up. *Ocean Eng.* **1992**, *19*, 75–79. [[CrossRef](#)]
30. Kriebel, D. Technical note nonlinear wave interaction with a vertical circular Cylinder: Wave forces. *Ocean Eng.* **1998**, *25*, 597–605.
31. Lykke Andersen, T.; Frigaard, P.; Damsgaard, M.L.; De Vos, L. Wave run-up on slender piles in design conditions Model tests and design rules for offshore wind. *Coast. Eng.* **2011**, *58*, 281–289. [[CrossRef](#)]
32. Morison, J.; Johnson, J.; Schaaf, S. The force exerted by surface waves on piles. *J. Pet Technol.* **1950**, *2*, 149–154. [[CrossRef](#)]
33. Ning, D.Z.; Zang, J.; Liu, S.X.; Taylor, R.E.; Teng, B.; Taylor, P.H. Free-surface evolution and wave kinematics for nonlinear uni-directional focused wave groups. *Ocean Eng.* **2009**, *36*, 1226–1243. [[CrossRef](#)]
34. Soares, C.G. *Offshore Structure Modeling*; World Scientific: Cambridge, MA, USA, 1995.
35. Fenton, J.D. *Nonlinear Wave Theories, the Sea*; Wiley: Hoboken, NJ, USA, 1990; Volume 9.
36. Taylor, R.E.; Hung, S. Second order diffraction forces on a vertical cylinder in regular waves. *Appl. Ocean Res.* **1987**, *9*, 19–30. [[CrossRef](#)]
37. Jin, R.; Teng, B.; Ning, D.Z.; Zhao, M.; Cheng, L. Numerical investigation of influence of wave directionality on the water resonance at a narrow gap between two rectangular barges. *Act. Oceanolo. Sin.* **2017**, *36*, 104–111. [[CrossRef](#)]
38. Zhou, B.Z.; Ning, D.Z.; Teng, B.; Bai, W. Numerical investigation of wave radiation by a vertical cylinder using a fully nonlinear HOBEM. *Ocean Eng.* **2013**, *70*, 1–13. [[CrossRef](#)]

**Disclaimer/Publisher’s Note:** The statements, opinions and data contained in all publications are solely those of the individual author(s) and contributor(s) and not of MDPI and/or the editor(s). MDPI and/or the editor(s) disclaim responsibility for any injury to people or property resulting from any ideas, methods, instructions or products referred to in the content.